The cubic structure of Li$_3$As stabilized by substitution – Li$_8$TtAs$_4$ (Tt = Si, Ge) and Li$_{14}$TtAs$_6$ (Tt = Si, Ge, Sn) and their lithium ion conductivity

Martin Schmid[a], Florian Wegner[a], Claudia De Giorgi[a], Florian Pielnhofer[a] and Arno Pfitzner*[a]

Supporting information

Table of Content

1.Synthesis

Figure S1. Powder diffraction data after ball mill experiment of $Li_{14}SiAs_6$ (black) and calculated intensities (red). Intensities marked with blue circles can be assigned to Li_3As.
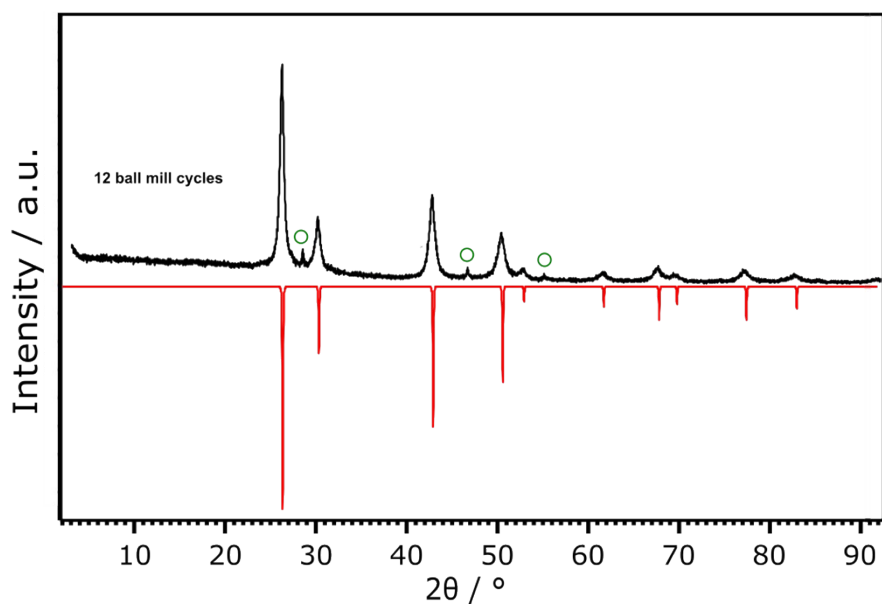
Figure S2. Powder diffraction data after ball mill experiment of $Li_{14}GeAs_6$ (black) and calculated intensities (red). Intensities marked with green circles can be assigned to unreacted Ge.
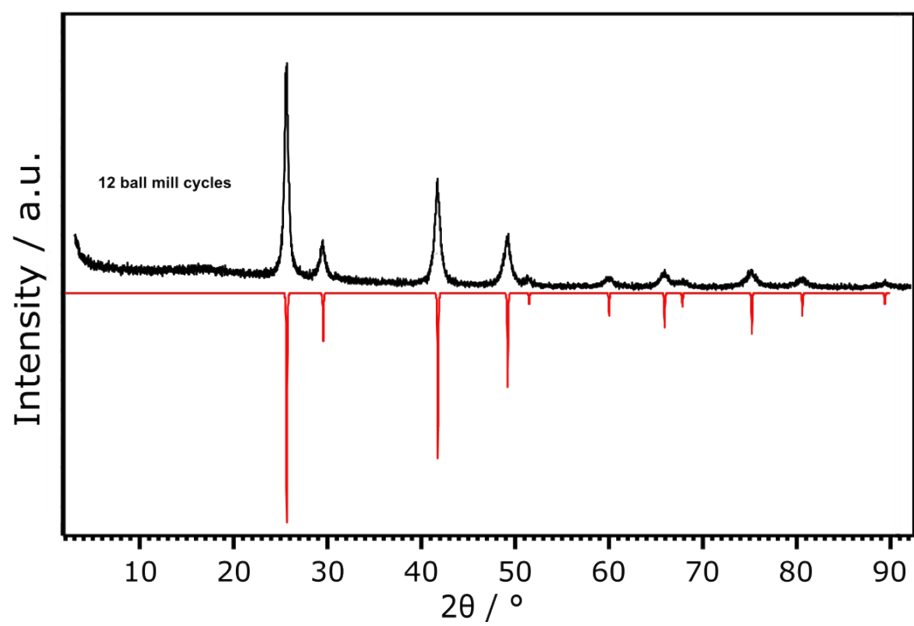
Figure S3. Powder diffraction data after ball mill experiment of $Li_{14}SnAs_6$ (black) and calculated intensities (red).

2.Crystallographic data and interatomic distances

2.1 Structure
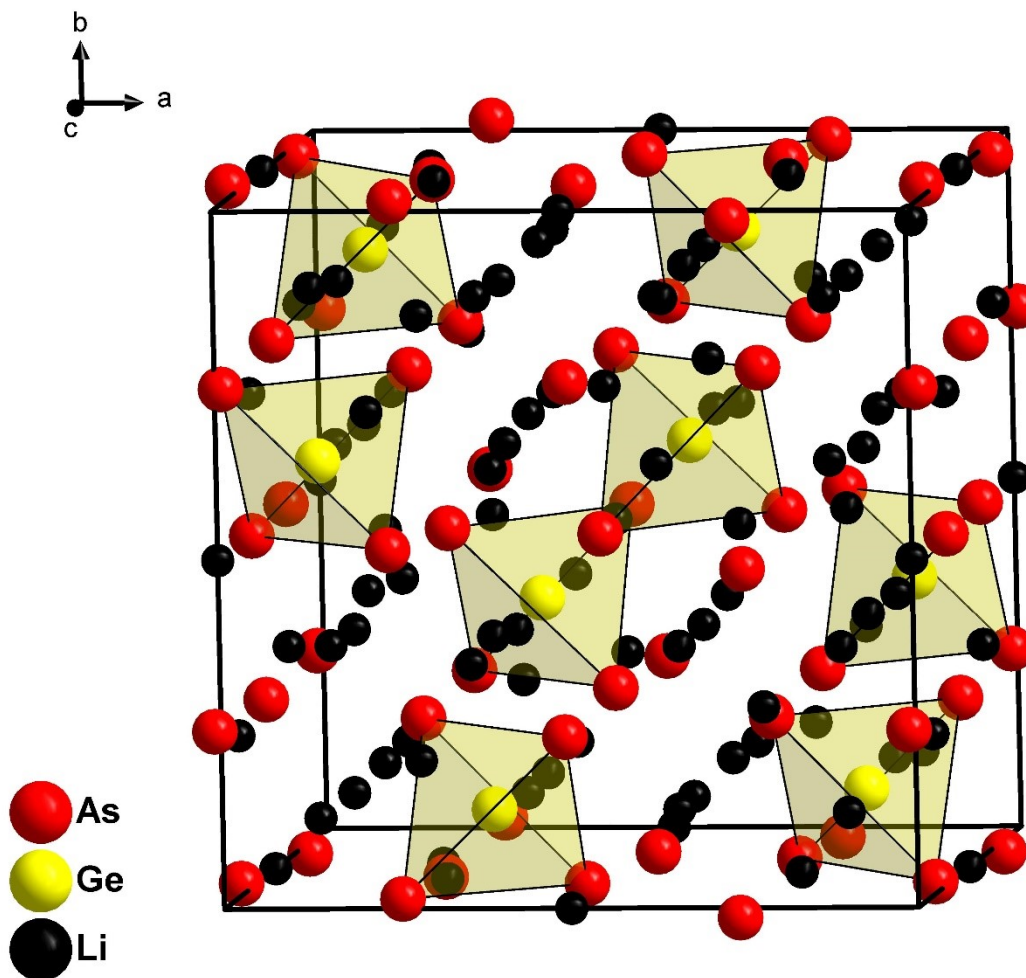
Figure S4. Cubic crystal structure of Li_8GeAs_4 with $[GeAs_4]^{8-}$-tetrahedra painted in yellow.

2.2 Refinement parameters

Table S1 Refinement parameters of Li_8SiAs_4, Li_8GeAs_4, $Li_{14}SiAs_6$, $Li_{14}GeAs_6$, $Li_{14}SnAs_6$ from Rietveld refinement at room temperature.

Empirical formula	$Li_{9.333}Si_{0.667}As_4$	$Li_{9.333}Ge_{0.667}As_4$	$Li_{9.333}Sn_{0.667}As_4$	Li_8SiAs_4	Li_8GeAs_4
T / K			293		
Rad. wavelength			$\lambda = 1.5406$ Å		
Θ range / deg.		2.00 – 90.545		2.00 – 91.985	
Crystal system			cubic		
Space group		$Fm\bar{3}m$ (No. 225)		$Pa\bar{3}$ (No. 218)	
Color	dark red	grey	grey	dark red	grey
a / Å	6.131(1)	6.143(1)	6.193(1)	12.096(1)	12.170(1)
V / Å^3	230.4(2)	231.8(1)	237.53(1)	1769.8(1)	1802.7(1)
Z	1	1	1	8	8
Formula weight / g mol^{-1}	383.2	412.8	443.6	383.3	427.8
ρ calc.) / g cm^{-3}	2.761	2.956	3.101	2.876	3.152
R_p	0.0483	0.0637	0.0445	0.0439	0.0608
R_{wp}	0.0603	0.0841	0.0580	0.0562	0.0877
R_{exp}	0.0364	0.0561	0.0409	0.0516	0.0820
R_{gt}, wR_{gt} ($I>3\sigma$)	0.0124, 0.0166	0.0265, 0.0328	0.0137, 0.0174	0.0169, 0.0222	0.0165, 0.0205
R_{all}, wR_{all}	0.0124, 0.0166	0.0265, 0.0328	0.0137, 0.0174	0.0229, 0.0236	0.0269, 0.0224
$\Delta\rho_{min}$, $\Delta\rho_{max}$ / eV	-0.16, 0.11	-0.22, 0.30	-0.10, 0.23	-0.31, 0.24	-0.31, 0.31
GOOF	1.66	1.50	1.42	1.09	1.07
Deposition number (CCDC)	2332050	2332051	2332049	2332048	2332047

2.3 Atomic positions and displacement parameters

Table S2 List of the atomic positions and corresponding displacement parameters from the Rietveld refined structures of Li_8SiAs_4 and Li_8GeAs_4.

Li_8SiAs_4	Wyck. position	x	y	z	U_{iso} / Å²	Occupancy / %
As1	24d	0.25969(7)	0.01653(7)	0.9912(3)	0.0208(4)	100
As2	8c	0.25849(3)	0.2585(3)	0.2585(3)	0.0215(12)	100
Si1	8c	0.6283(6)	0.6283(6)	0.6283(6)	0.0151(16)	100
Li1	4b	1/2	1/2	1/2	0.030(4)	100
Li2	8c	0.113(3)	0.130(4)	0.868(3)	0.030(4)	100
Li3	24d	0.130(4)	0.130(4)	0.130(4)	0.030(4)	100
Li4	24d	0.139(4)	0.131(3)	0.370(3)	0.030(4)	100
Li5	24d	0.00(3)	0.26(3)	0.759(5)	0.030(4)	16.67
Li_8GeAs_4		x	y	z	U_{iso} / Å²	Occupancy / %
As1	24d	0.25613(12)	0.01329(11)	0.9930(3)	0.0115(7)	100
As2	8c	0.2553(3)	0.2553(3)	0.2553(3)	0.020(2)	100
Ge1	8c	0.6275(3)	0.6275(3)	0.6275(3)	0.0112(9)	100
Li1	4b	1/2	1/2	1/2	0.036(6)	100
Li2	8c	0.123(4)	0.116(4)	0.878(4)	0.036(6)	100
Li3	24d	0.141(3)	0.141(3)	0.141(3)	0.036(6)	100
Li4	24d	0.142(5)	0.137(4)	0.375(4)	0.036(6)	100
Li5	24d	0.982(84)	0.215(16)	0.710(12)	0.036(6)	16.67

Table S3 List of the atomic positions and displacement parameters for $Li_{14}SiAs_6$, $Li_{14}GeAs_6$, and $Li_{14}SnAs_6$ from Rietveld refinements.

$Li_{14}SiAs_6$	Wyck. position	x	y	z	U_{iso} / Å²	Occupancy / %
As1	4a	0	0	0	0.03282(14)	100
Si1	8c	1/4	1/4	1/4	0.0448(7)	8.33
Li1	8c	1/4	1/4	1/4	0.0448(7)	91.67
Li2	4b	1/2	0	0	0.101(4)	50
$Li_{14}GeAs_6$		x	y	z	U_{iso} / Å²	Occupancy / %
As1	4a	0	0	0	0.0396(2)	100
Ge1	8c	1/4	1/4	1/4	0.0473(8)	8.33
Li1	8c	1/4	1/4	1/4	0.0473(8)	91.67
Li2	4b	1/2	0	0	0.192(14)	50
$Li_{14}SnAs_6$		x	y	z	U_{iso} / Å²	Occupancy / %
As1	4a	0	0	0	0.01797(13)	100
Sn1	8c	1/4	1/4	1/4	0.0283(3)	8.33
Li1	8c	1/4	1/4	1/4	0.0283(3)	91.67
Li2	4b	1/2	0	0	0.198(8)	50

2.4 Coordination polyhedra
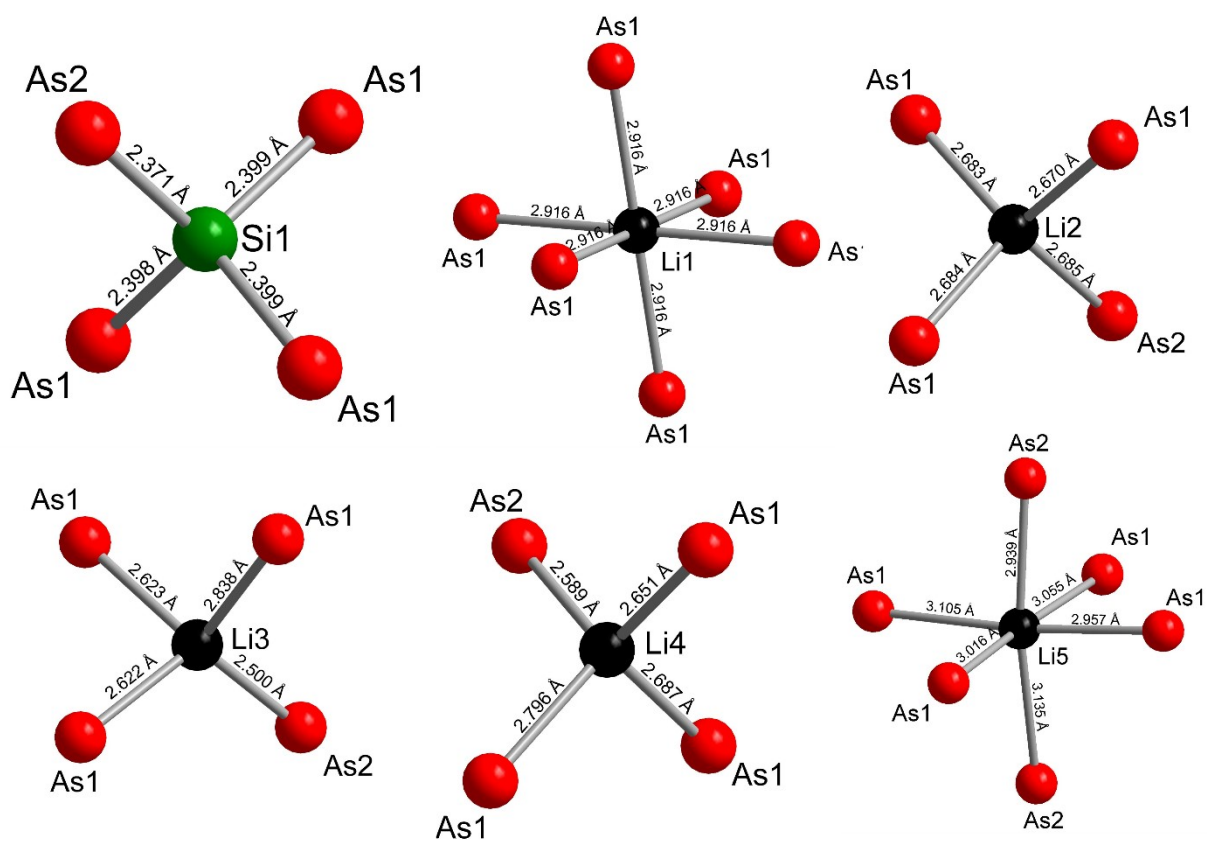
Figure S5. Selected coordination polyhedra in Li_8SiAs_4.
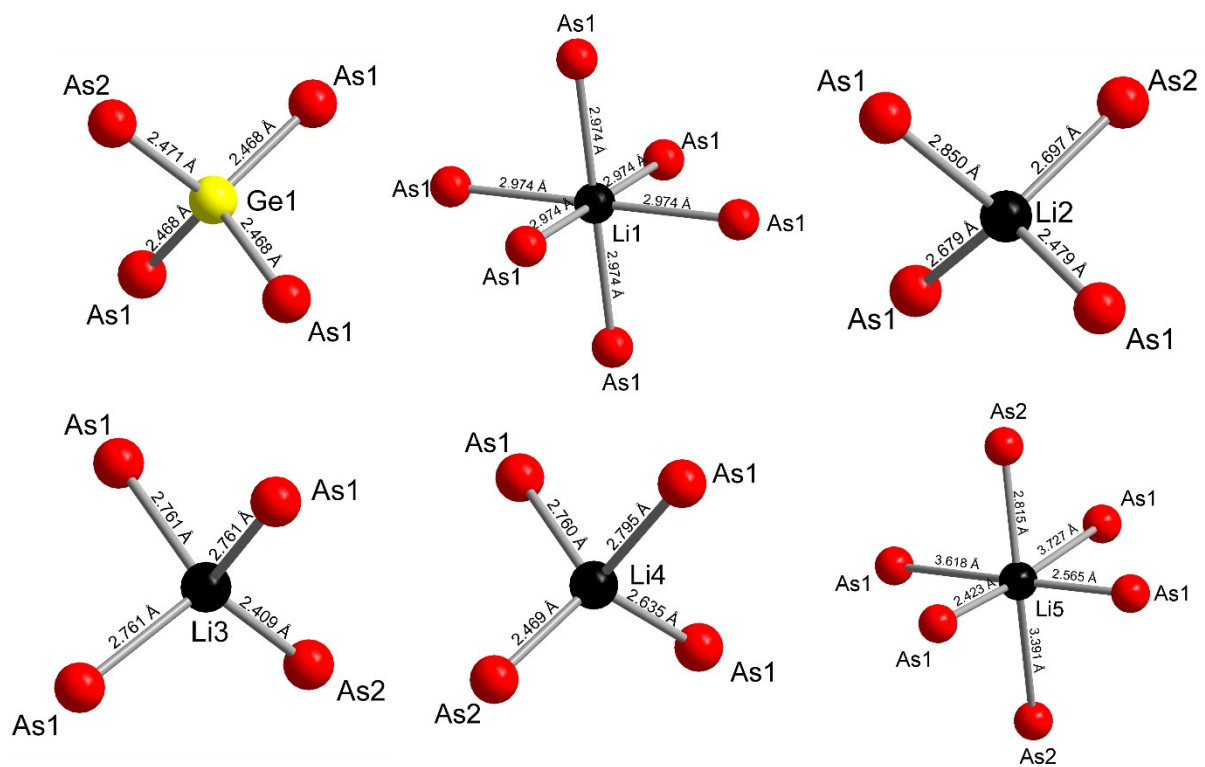
Figure S6. Selected coordination polyhedra in Li₈GeAs₄.
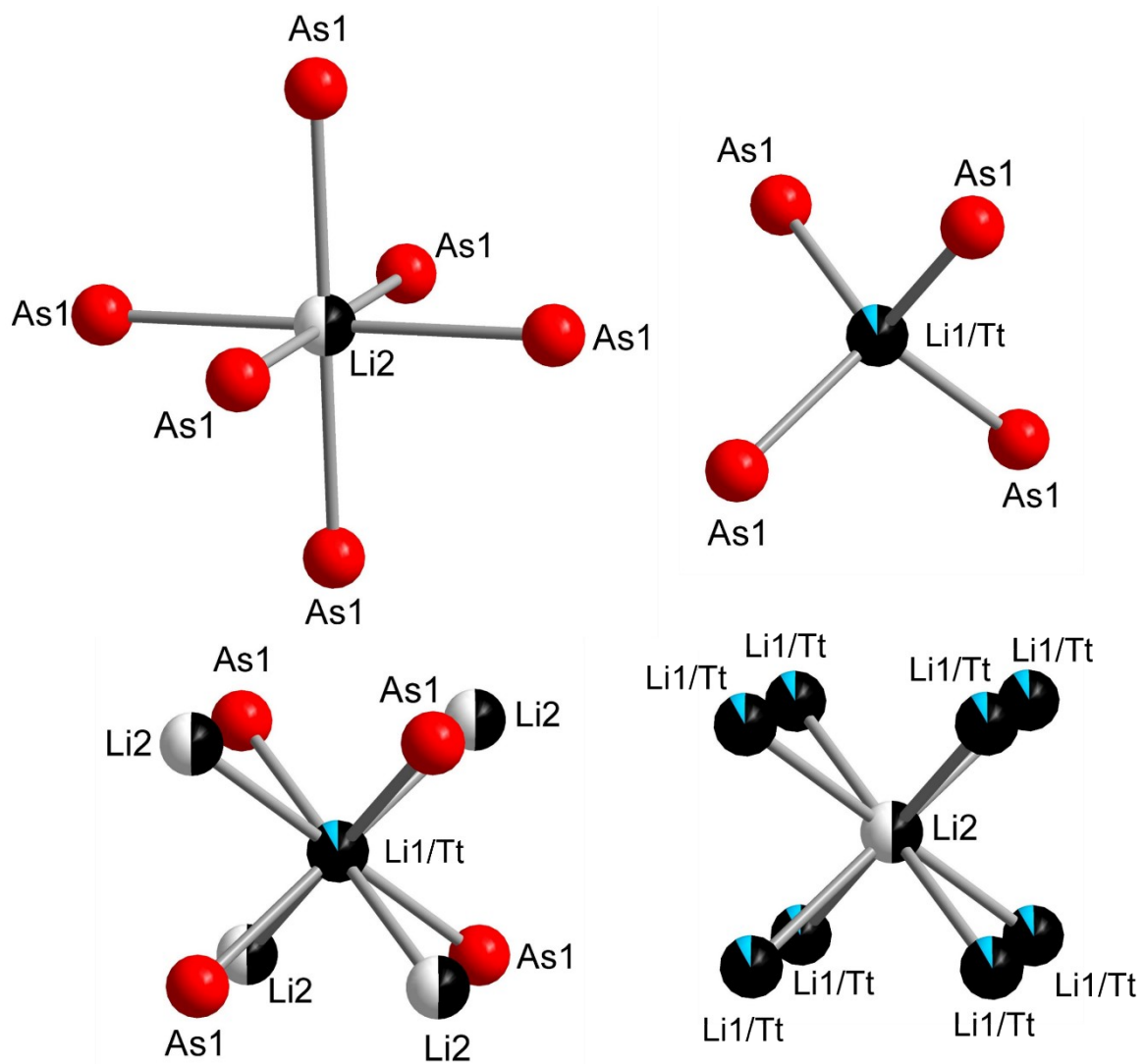
Figure S7. Selected coordination polyhedra in Li$_{14}$*Tt*As$_6$ (*Tt* = Si, Ge, Sn). Interatomic distances for each compound are given in Table 1.

2.5 Powder diffraction data and Rietveld refinement
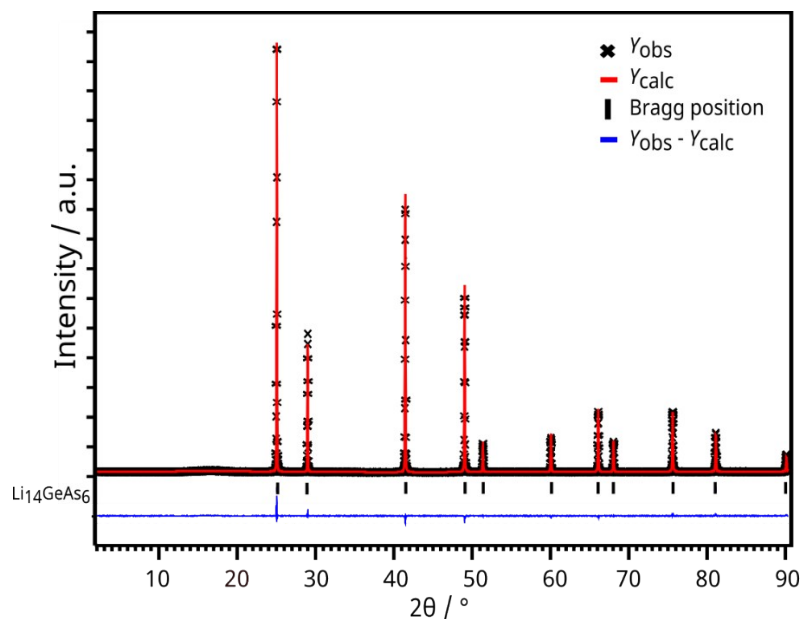
Figure S8. X-ray powder diffraction data with Rietveld analysis of $Li_{14}GeAs_6$. Observed intensities Y_{obs} are displayed with black crosses, the red line indicates the calculated intensities Y_{calc}, Bragg positions are marked with black lines and the difference plot (Y_{obs}- Y_{calc}) is drawn in blue.
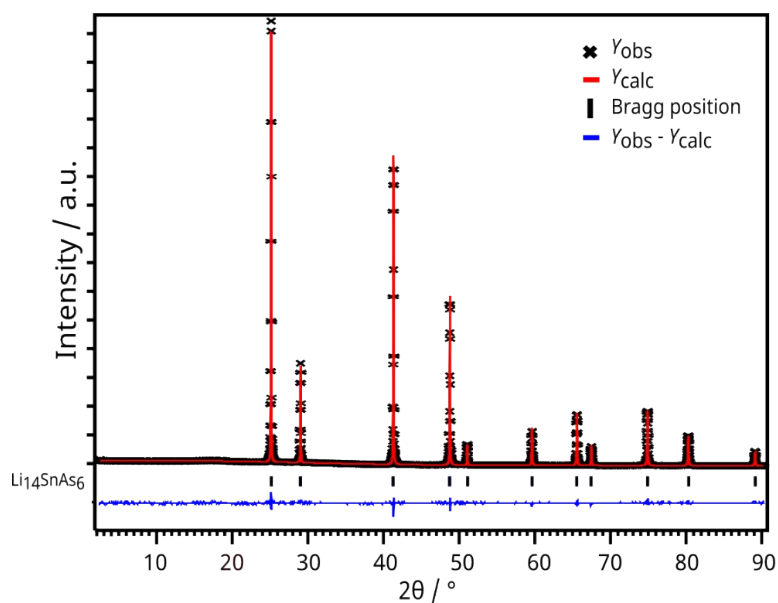
Figure S9. X-ray powder diffraction data with Rietveld analyses of $Li_{14}SnAs_6$. Observed intensities Y_{obs} are displayed with black crosses, the red line indicates the calculated intensities Y_{calc}, Bragg positions are marked with black lines and the difference plot (Y_{obs}- Y_{calc}) is drawn in blue.

Rietveld refinement

The proposed structure solution of $Li_{14}TtAs_6$ (Tt = Si, Ge, Sn) were achieved using X-Ray powder diffraction data. Since no sufficient amounts of powder were feasible to perform neutron powder diffraction, several limitations occur regarding the structure solution using XRPD-data. The occupancy distribution of the tetrahedral void by lithium and tetrel cation in the ratio of 1:11 was fixed according to the stochiometric amount of tetrel and lithium weight in, since the electron density of Si and Li is not distinguishable on the same crystallographic position by XRPD. The absence of side phases and lowest residual values for the proposed distribution support this solution. Further the distribution of lithium content on the Li1 position in the tetrahedral voids and the Li2 position in the octahedral voids is indirectly connected with the ratio of lithium and tetrel cation in the tetrahedral voids and therefore was set to a S.O.F of 0.5 in accordance with the principle of electroneutrality and good agreement with residual electron density.

3. Thermal analysis

3.1 High temperature powder diffraction data
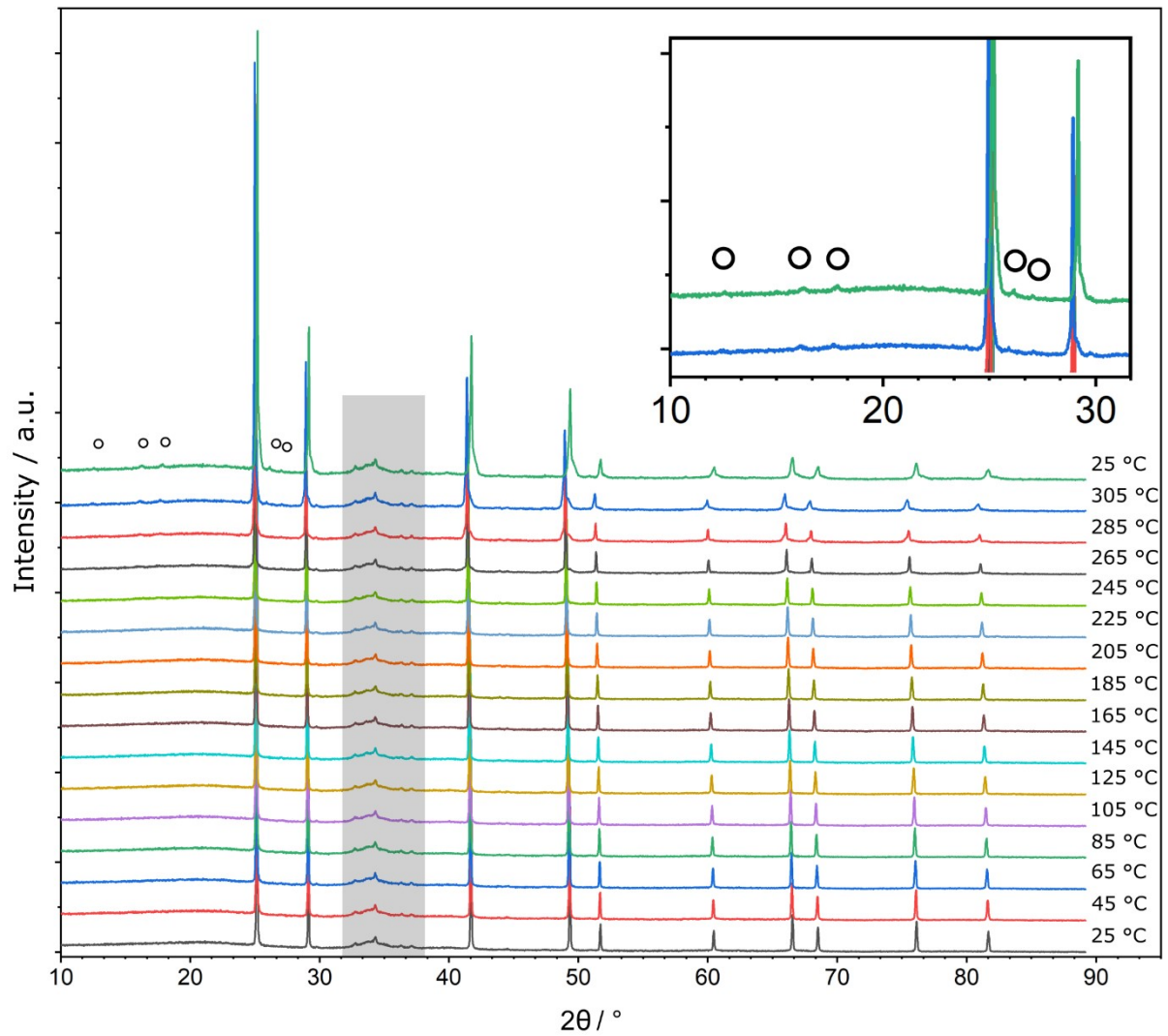
Figure S10. High temperature powder diffraction data (25 °C -> 305 °C -> 25 °C) of $Li_{14}SiAs_6$ in steps of 20 °C. Additional reflexes are emerging at a temperature of 305 °C which can be assigned to Li_3As and Li_8SiAs_4 (marked with a circle). Please note that artefacts of the heating device are present in a 2θ range of 32 ° - 38 ° (grey background).
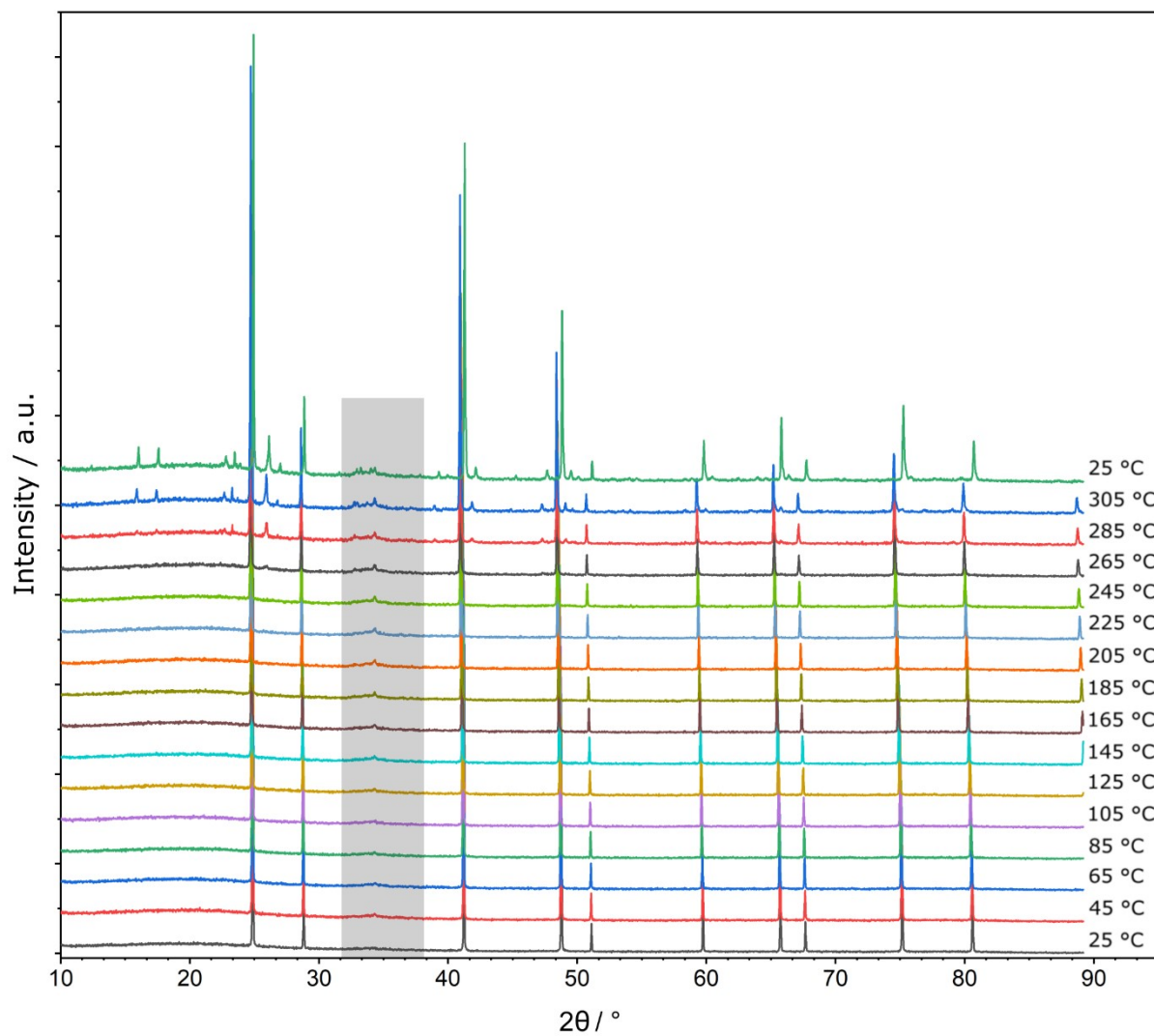
Figure S11. High temperature powder diffraction data (25 °C -> 305 °C -> 25 °C) of $Li_{14}SnAs_6$ in steps of 20 °C. Additional reflections are emerging at a temperature of 285 °C which can be assigned to Li_3As and formal Li_8SnAs_4. Please note that artefacts of the heating device are present in a 2θ range of 32 ° - 38 ° (grey background).
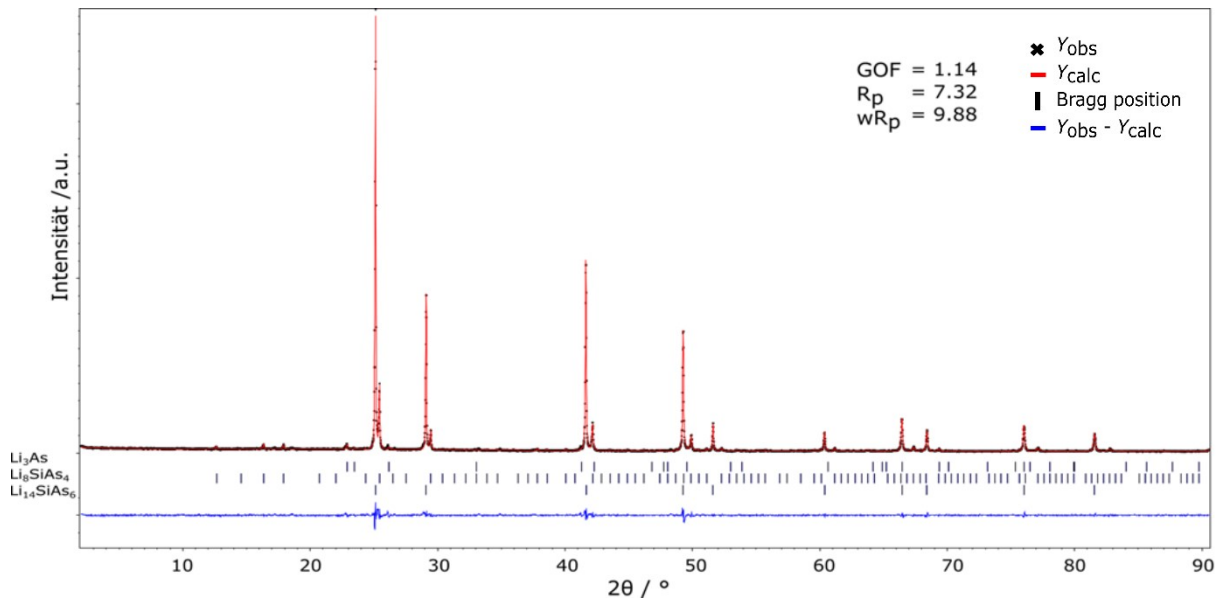
Figure S12. Powder X-Ray diffraction data of $Li_{14}SiAs_6$ after DTA with indexed reflections. Observed intensities Y_{obs} are displayed with black crosses, the red line indicates the calculated intensities Y_{calc}, Bragg positions are marked with black lines and the difference plot (Y_{obs}- Y_{calc}) is drawn in blue. Due to decomposition prosses of $Li_{14}SiAs_4$ (indexed with a = 6.126(1) Å) the two phases Li_3As (indexed with a = b = 4.362(1) Å and c = 7.773(1) Å) and Li_8SiAs_4 (indexed with a = 12.107(1) Å) are present.
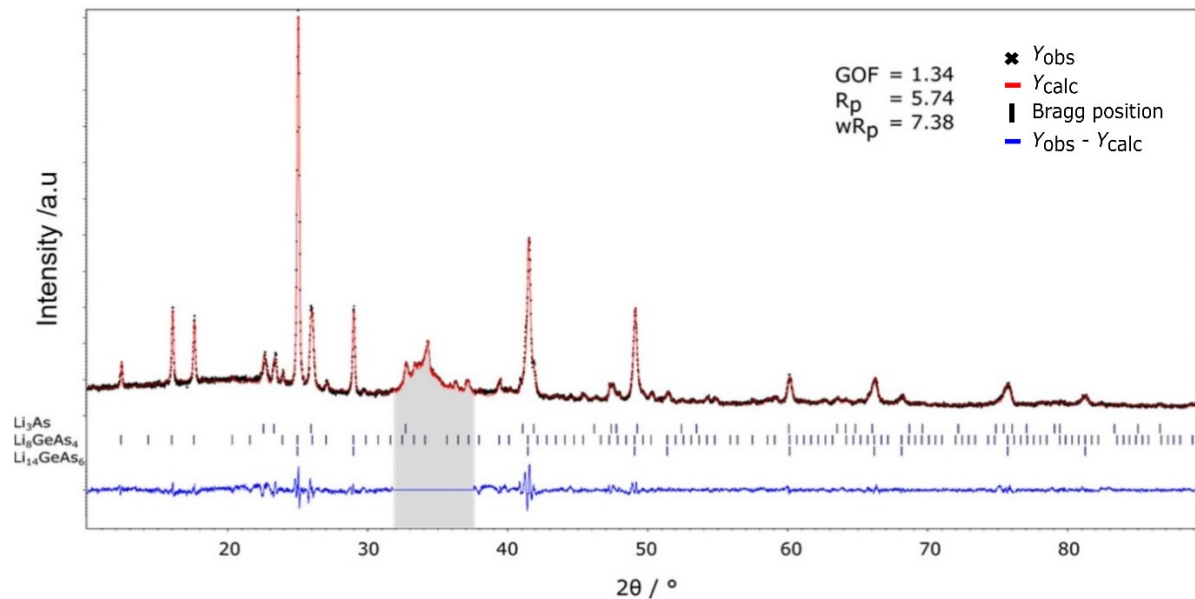
Figure S13. Powder X-Ray diffraction data of $Li_{14}GeAs_6$ at 305 °C with indexed reflections. Observed intensities Y_{obs} are displayed with black crosses, the red line indicates the calculated intensities Y_{calc}, Bragg positions are marked with black lines and the difference plot (Y_{obs}- Y_{calc}) is drawn in blue. Because of artefacts of the heating device, the 2θ range from 32 ° - 38 ° is excluded from analysis (grey background). Due to decomposition processes of $Li_{14}GeAs_4$ (indexed with a = 6.142(1) Å) the two phases Li_3As (indexed with a = b = 4.384(1) Å and c = 7.783(1) Å) and Li_8GeAs_4 (indexed with a = 12.284(1) Å) are present.

3.2 Differential thermal analysis (DTA)
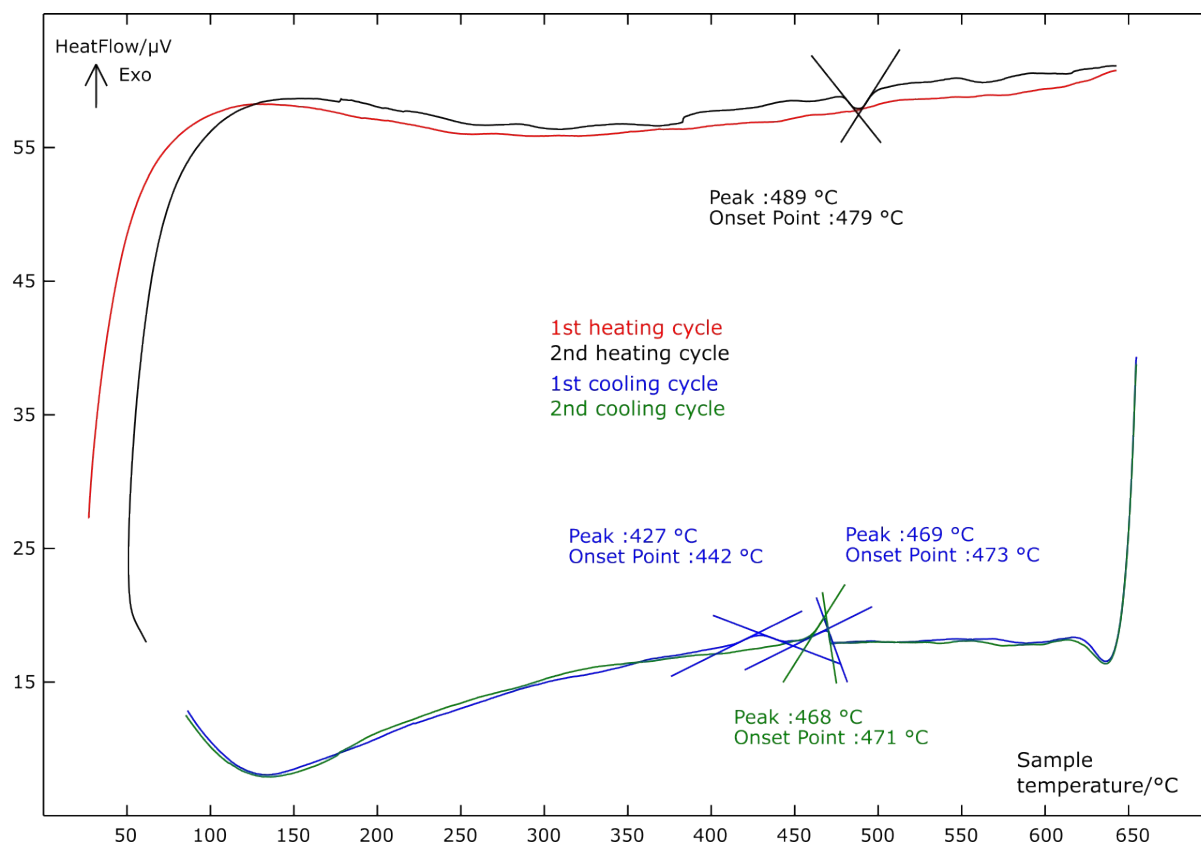
Figure S14. Differential thermal analysis (DTA) of $Li_{14}SiAs_6$ showing endothermal effects in the heating cycles (red and black) and exothermal effects in the cooling cycles (blue and green). It should be noted that our DTA machine shows some small artefacts similar to the weak peaks in the 2nd heating cycle. Therefore, we do not assign any thermal effects to these signals.
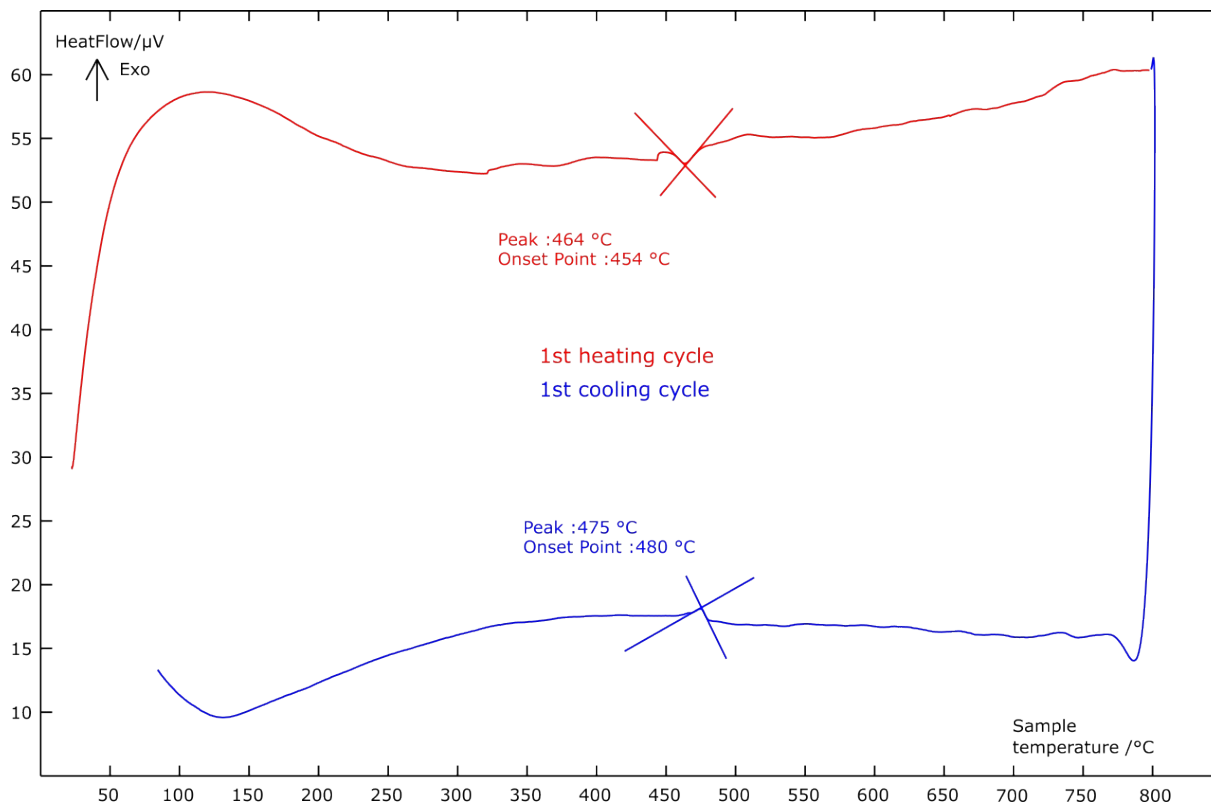
Figure S15. Differential thermal analysis (DTA) of $Li_{14}GeAs_6$ showing one endothermal effect in the heating cycle (red) and one exothermal effect in the cooling cycle (blue). Because of high corrosion of the silica glass ampoule only one heating and cooling cycle was measured. It should be noted that our DTA machine shows some small artefacts similar to the weak peaks in the heating cycle. Therefore, we do not assign any thermal effects to these signals.
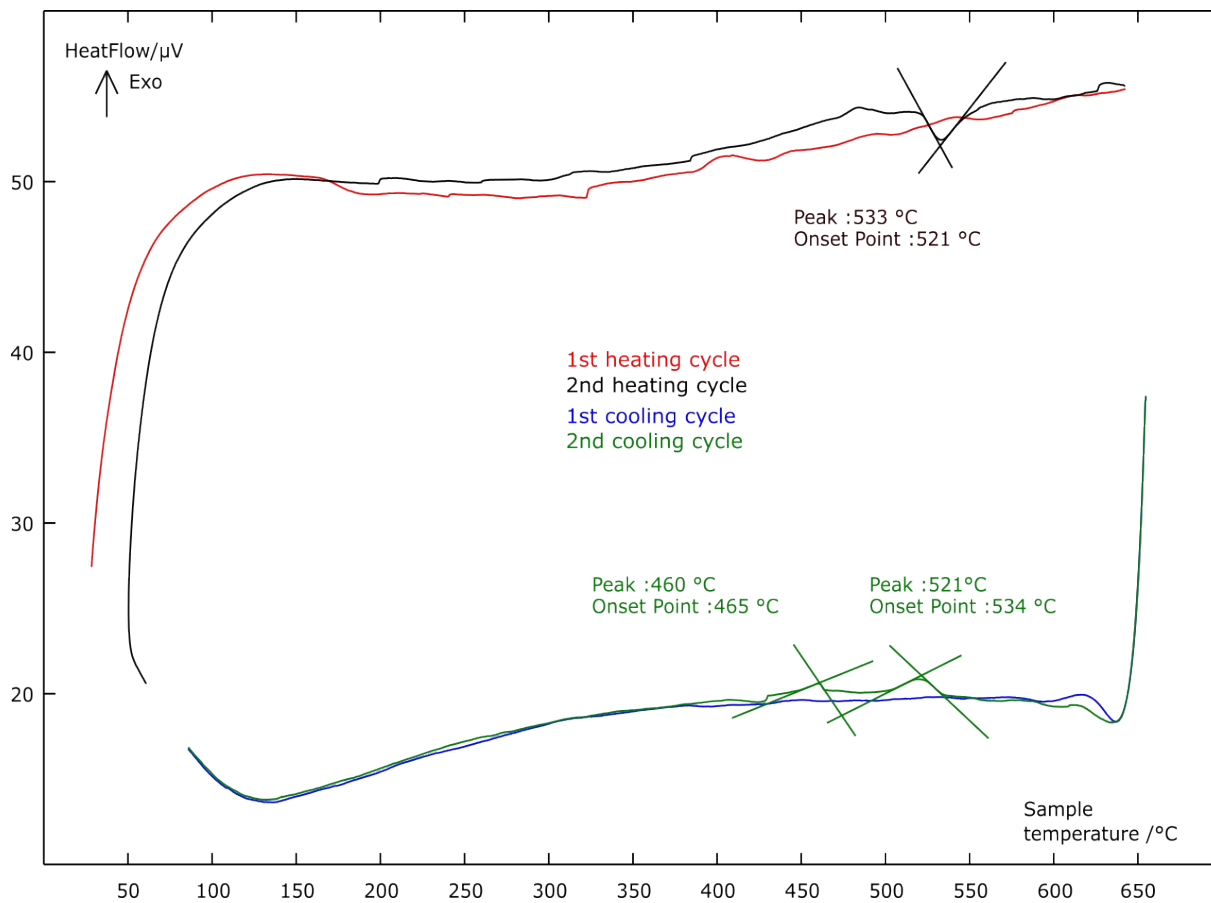
Figure S16. Differential thermal analysis (DTA) of $Li_{14}SnAs_6$ showing endothermal effects in the heating cycles (red and black) and exothermal effects in the cooling cycles (blue and green). It should be noted that our DTA machine shows some small artefacts similar to the weak peaks in the 2nd heating cycle. Therefore, we do not assign any thermal effects to these signals.

4.Conductivity experiments

Conductivity measurements were carried out by a Zahner Zennium impedance analyser connected with an in-house designed cell. The samples were prepared by applying pressure (6 t) on the powder to form cylindrical pellets (Ø = 8 mm) with densities of 80% ($Li_{14}SiAs_6$), 80% ($Li_{14}GeAs_6$), 88% ($Li_{14}SnAs_6$), 83% (Li_8SiAs_4) and 81% (Li_8GeAs_4). The pellets were contacted using indium foil. Current was collected by platin electrodes placed between the indium foil and corundum spaces which isolates the contacts from the environment (corundum // platin contact // indium foil // sample // indium foil // platin contact // corundum). Impedance measurements were performed by two heating and two cooling cycles in a temperature range of 50 °C – 100 °C in steps of 10 °C. Samples were kept at the measuring temperature for at least 20 minutes for ensuring thermal equilibrium. The frequency of the applied excitation voltage (50 mV) was swept starting from 1 MHz to 100 mHz. For determining the lithium ion mobility only data from the last cooling cycle was used sparing out the previous heating and the first cooling cycle, because the ongoing sintering process between the sample and the indium contacts led to better data quality for the last cooling cycle. To retrieve the real resistance values from the Nyquist plots the low frequency tails were extrapolated to intersect with the x axis followed by a correction of the geometrical parameters and density of the sample pellets. The Nyquist plot of Li_8GeAs_4 shows a second semicircle embedded in the low frequency tail between the fist semicircle and the low frequency tail which can be possibly assigned to grain boundaries.
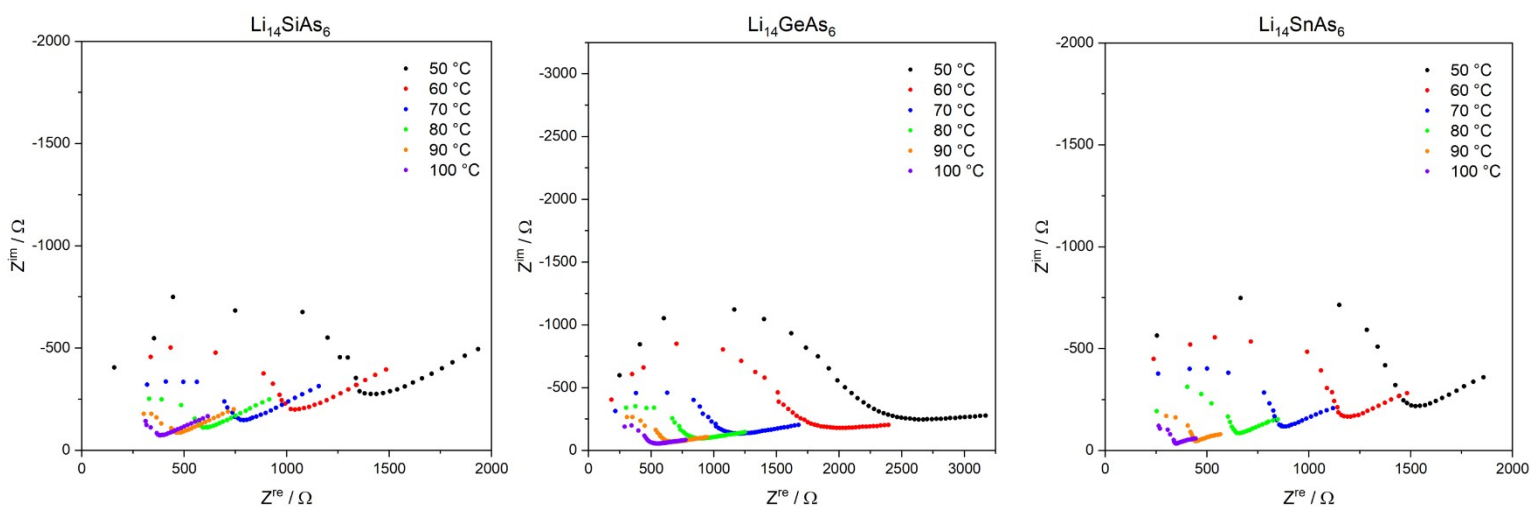
Figure S17. Nyquist plots of the compounds $Li_{14}SiAs_6$, $Li_{14}GeAs_6$ and $Li_{14}SnAs_6$ (left to right) in the temperature range of 50 °C – 100 °C.
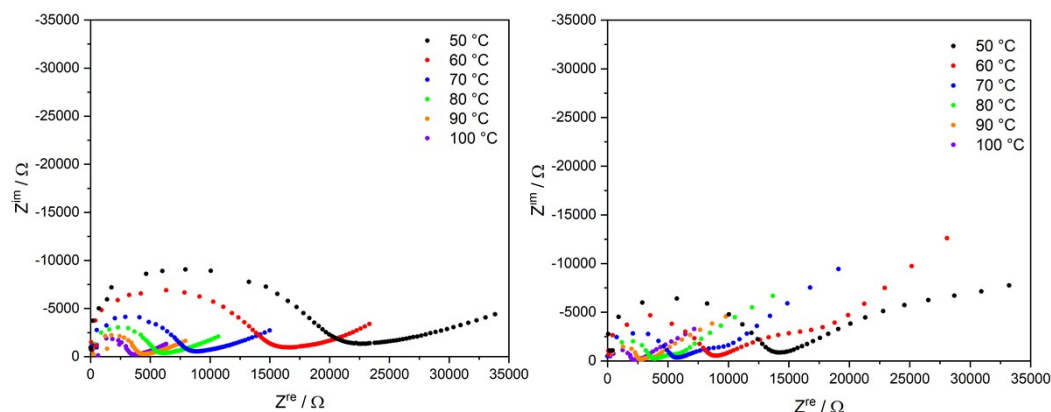
Figure S18. Nyquist plots of the compounds Li_8SiAs_4(left) and Li_8GeAs_4(right) in the temperature range of 50 °C – 100 °C.